IEEE Access
Multidisciplinary ⋮ Rapid Review ⋮ Open Access Journal

Received December 1, 2020, accepted December 28, 2020, date of publication January 5, 2021, date of current version January 14, 2021.

Digital Object Identifier 10.1109/ACCESS.2021.3049271

Design and Fabrication of Magnetic System Using Multi-Material Topology Optimization

TAEHOON JUNG, JAEJOON LEE, AND JAEWOOK LEE
School of Mechanical Engineering, Gwangju Institute of Science and Technology, Gwangju 61005, South Korea

Corresponding author: Jaewook Lee (jaewooklee@gist.ac.kr)

This research was supported by a grant (20TLRP-C135448-04, Development of Hybrid Electric Vehicle Conversion Kit for Diesel Delivery Trucks and its Commercialization for Parcel Services) from Transportation & Logistics Research Program (TLRP) funded by Ministry of Land, Infrastructure and Transport of Korean government.

ABSTRACT This paper presents the design and fabrication schemes of a magnetic system consisting of segmented permanent magnet (PM) blocks, back-iron and frame structures. Here, a frame structure aims to bind PM blocks and iron structure. Non-intuitive design of segmented PMs and back-iron are obtained using multi-material topology optimization formulation. Subsequently, a non-magnetic frame structure is designed through a post-processing procedure, which is proposed using the smoothed fields of optimized PM and back-iron densities. Final design results are converted into computer-aided design (CAD) models and fabricated using conventional or additive manufacturing techniques. Segmented PM blocks, and back-iron structures are processed using water-jet cutting and wire electrical discharge machining, respectively. A frame structure is fabricated by additive manufacturing using a multi-jet printing machine. Using the proposed schemes, two magnetic systems are successfully designed and fabricated, respectively, for maximizing the magnetic field inside a rectangular cavity, and maximizing the magnetic force generated with a C-core electromagnet.

INDEX TERMS Design optimization, permanent magnets, iron, finite element methods, magnetic devices, magnetic forces.

I. INTRODUCTION

A magnetic system combining permanent magnets (PMs) and back-iron structure is a key component used in a wide range of applications. In actuators, electric motors, nuclear-magnetic-resonance (NMR), magnetic-resonance-imaging (MRI), etc., the design of magnetic system determines main device performances. Structural topology optimization is an effective design tool that can produce non-intuitive design (i.e. structural shape and configuration) for a given design goal. Since it was first proposed in structural stiffness problems [1], topology optimization has been successfully extended to various physical disciplines [2] such as thermal fluid [3], and electromagnetic problems [4], [5].

Vigorous topology optimization studies have been carried out on the design of PM and back-iron structures in a magnetic system. In [6], a PM with continuously varying magnetization direction is designed by setting a magnetization direction as a design variable of topology optimization. Such a PM is not preferred due to difficulties in fabrication. Instead, it can be manufactured as a combination of segmented PM blocks with uniform magnetization directions. For the design of segmented PM blocks, topology optimization using additional density design variables was proposed in [7]. In [8], the isoparametric projection approach was applied for the design of segmented PM blocks. In [9], segmented PMs were designed using topology optimization considering finite coercivity of PM material. In [10], [11], three-dimensional segmented PMs were designed, respectively, using the virtual-magnet approach and topology optimization with penalization scheme. Structural topology optimization for the simultaneous design of segmented PMs and back-irons has been proposed in [12]–[16]. In these studies, the shape of configuration of a magnetic system consisting of segmented PM blocks and back-iron structure are co-designed using multi-material topology optimization formulation.

Despite numerous studies on topology optimization for magnetic system design, few studies have demonstrated the fabrication of a magnetic system that are designed using topology optimization. In [17], [18], single PM block with fixed magnetization direction are fabricated

The associate editor coordinating the review of this manuscript and approving it for publication was Montserrat Rivas.

using additive manufacturing of polymer-bonded magnets. A review paper [19] summarizes studies on additive manufacturing of PMs, back-irons, coils (i.e. three magnetic components of electric machines). In [19], several fabrication examples of magnetic cores (i.e. back-irons) designed through topology optimization are presented. None of previous studies have conducted the fabrication of a magnetic system consisting of segmented PM blocks and back-irons designed using topology optimization. More efforts are required on the manufacturing of magnetic system design results that are obtained using topology optimization.

Accordingly, the present work aims to present the fabrication of a magnetic system designed using multi-material topology optimization. Here, a magnetic system is composed of not only segmented PM blocks, back-iron structure, but also a non-magnetic frame structure for binding PMs and back-irons. A three-field density formulation proposed in [15], [16] is modified and applied for the shape and configuration of PM and back-iron structures. In the present work, the non-linear B-H relation of soft ferromagnetic material (i.e. back-iron) is included in multi-material topology optimization, which was not considered in [15], [16]. PM segmentation is carried out using an orientation penalization scheme proposed in [11]. A frame structure is next designed using a post-processing scheme proposed in the present work. A frame structure serves to surround and bind PMs and back-irons. For this, a frame structure is designed as the boundary of designed PMs and back-iron structures, which is identified from the smoothed fields of PM and back-iron densities. In addition, PM blocks and back-iron structures are adjusted to fit a designed frame structure through the proposed post-processing scheme.

The final design result obtained after a post-processing procedures is converted into computer-aided design (CAD) model, and fabricated using conventional or additive manufacturing techniques. Appropriate manufacturing techniques for each component of a magnetic system is chosen considering material characteristics and manufacturing conveniences. In the present work, segmented PM blocks are made of Barium ferrite, and fabricated using water-jet cutting machining. Back-iron structures are made of low carbon steel, and fabricated using wire electrical discharge machining. A frame structure is fabricated by additive manufacturing using a multi-jet printing machine with ultraviolet curing plastic material. The proposed design and fabrication approaches are applied to two magnetic system examples. The first example aims to design and fabricate a magnetic system for maximizing the magnetic field inside a rectangular cavity. In the second example, a magnetic system is designed and fabricated for maximizing the magnetic force generated with a C-core electromagnet.

The remaining paper is organized as follows. Section II explains the formulation of multi-material topology optimization proposed for a magnetic system design. Section III describes manufacturing techniques used for the fabrication of design results. In Section IV, two design and fabrication examples are provided to confirm the effectiveness of the proposed schemes. Finally, conclusions are provided in Section V.

II. MULTI-MATERIAL TOPOLOGY OPTIMIZATION

This section explains multi-material topology optimization proposed for the design of a magnetic system that is composed of PM segments, back-iron, and non-magnetic frame structure. The interpolation functions between design variables and material properties (i.e. magnetic permeability and remanence) are first explained. Next, a penalization scheme for the PM segmentation is explained, followed by the explanation of an optimization strategy. Finally, a post-processing scheme proposed for the design of a non-magnetic frame structure is demonstrated.

A. MATERIAL INTERPOLATION SCHEME

The governing equation of a magnetostatic analysis including PM and back-iron materials is derived from the Maxwell's equations with the vector potential $\vec{A}$ formulation as

$$\nabla \times \left(\frac{1}{\mu_r \mu_0} \nabla \times \vec{A} \right) = \nabla \times \left(\frac{1}{\mu_r \mu_0} \vec{B}_{\mathrm{r}} \right). \tag{1}$$

where μ_r is the relative magnetic permeability, μ_0 is the vacuum permeability (i.e. $4\pi \times 10^{-7}$ N/A^2), and $\vec{B}_r$ is the remanence of the PM material (i.e. the PM residual magnetic flux density). From the solution of (1) (i.e. the vector potential $\vec{A}$), the magnetic flux density, $\vec{B}$, is calculated as $\vec{B} = \nabla \times \vec{A}$. For multi-material topology optimization including PM magnetization direction design, a three-field density formulation proposed in [15], [16] is modified and applied in the present work. A design variable vector field $\vec{d}$ at position $\vec{x}$ is first defined as

$$\vec{d}(\vec{x}) = \begin{bmatrix} \phi_1(\vec{x}) \\ \phi_2(\vec{x}) \\ \zeta(\vec{x}) \\ \eta(\vec{x}) \end{bmatrix}, \tag{2}$$

with bounds $\phi_1(\vec{x}) \in [-1, 1]$, $\phi_2(\vec{x}) \in [-1, 1]$, $\zeta(\vec{x}) \in [-1, 1]$, and $\eta(\vec{x}) \in [-1, 1]$.

In (2), the design variables $\phi_1(\vec{x})$ and $\phi_2(\vec{x})$ are projected into the density fields that determine the structural topology of PM and back-iron materials. A Helmholtz filtering [20], [21] is applied to the variables $\phi_1(\vec{x})$ and $\phi_2(\vec{x})$:

$$-R_\phi^2 \begin{bmatrix} \nabla^2 \tilde{\phi}_1(\vec{x}) \\ \nabla^2 \tilde{\phi}_2(\vec{x}) \end{bmatrix} + \begin{bmatrix} \tilde{\phi}_1(\vec{x}) \\ \tilde{\phi}_2(\vec{x}) \end{bmatrix} = \begin{bmatrix} \phi_1(\vec{x}) \\ \phi_2(\vec{x}) \end{bmatrix}, \tag{3}$$

where R_ϕ is a parameter for filter radius. From the smoothed filtered design variables $\tilde{\phi}_1(\vec{x})$ and $\tilde{\phi}_2(\vec{x})$, the material density fields $\rho_1(\vec{x})$, and $\rho_2(\vec{x})$ are defined as

$$\begin{bmatrix} \rho_1(\vec{x}) \\ \rho_2(\vec{x}) \end{bmatrix} = \begin{bmatrix} H_r\left(\tilde{\phi}_1(\vec{x})\right) \\ H_r\left(\tilde{\phi}_2(\vec{x})\right) \end{bmatrix}. \tag{4}$$

In (4), a regularized Heaviside step function H_r [20] is defined as:

$$H_r(x) = \begin{cases} 0 & (x < -h) \\ \frac{1}{2} + \frac{15}{16}(\frac{x}{h}) - \frac{5}{8}(\frac{x}{h})^3 + \frac{3}{16}(\frac{x}{h})^5 & (-h \le x \le h) \\ 1 & (h < x) \end{cases}, \tag{5}$$

where h is a bandwidth parameter.

Next, the design variables $\zeta(\vec{x})$ and $\eta(\vec{x})$ in (2) are projected into a orientation vector field that determine the PM magnetization direction. The orientation vector field $\vec{\vartheta}(\vec{x})$ is defined as the directional cosines of the vector composed of design variables $\zeta(\vec{x})$ and $\eta(\vec{x})$:

$$\vec{\vartheta}(\vec{x}) = \begin{bmatrix} \vartheta_x(\vec{x}) \\ \vartheta_y(\vec{x}) \end{bmatrix} = \frac{1}{\sqrt{\zeta(\vec{x})^2 + \eta(\vec{x})^2 + \epsilon_0}} \begin{bmatrix} \zeta(\vec{x}) \\ \eta(\vec{x}) \end{bmatrix}, \tag{6}$$

where ϵ_0 is an infinitesimal number to avoid the singularity, which is set to 10^{-6} in the present work. It is noted that the orientation vector field $\vec{\vartheta}(\vec{x})$ defined in (6) automatically satisfies the unity magnitude condition (i.e. $\|\vec{\vartheta}(\vec{x})\| = 1$) that is required for orientation representation in the Cartesian coordinate system [11].

The structural topology and magnetization direction of PM material can be designed by determining the distribution of the PM remanence $\vec{B}_r$ in (1). For this, the PM remanence at position $\vec{x}$ is interpolated as

$$\vec{B}_r(\vec{x}) = \bar{B}_r\big(\rho_1(\vec{x})^p\big)\big(1 - \rho_2(\vec{x})^p\big)\vec{\vartheta}(\vec{x}), \tag{7}$$

where $\bar{B}_r$ is the magnitude of PM remanence, and p is the density penalty parameter, which is set to 3 in the present work. In (7), the PM structural topology is determined by two density fields ρ_1 and ρ_2 in (4), and the PM magnetization direction is determined by the orientation vector field $\vec{\vartheta}(\vec{x})$ in (6). Next, the structural topology of the back-iron material is designed by determining the distribution of the relative magnetic permeability μ_r in (1). For this, the permeability μ_r at position $\vec{x}$ is interpolated as

$$\mu_r(\vec{x}) = \rho_1(\vec{x})^p\big(\rho_2(\vec{x})^p\mu_r^{iron} + (1 - \rho_2(\vec{x})^p)\mu_r^{PM}\big) + \big(1 - \rho_1(\vec{x})^p\big)\mu_r^{air}, \tag{8}$$

where μ_r^{iron}, μ_r^{PM}, and mu_r^{air} are the relative magnetic permeability of iron, PM, and air, respectively. An iron relative permeability μ_r^{iron} in (8) is set as a nonlinear function with respect to the magnetic flux density to consider the saturation effect of soft ferromagnetic materials. The present work applies the non-linear B-H relation approximated by an exponential function [22]. In addition, a PM relative permeability μ_r^{PM} and air relative permeability μ_r^{air} are set to 1.05 and 1, respectively. In (8), p is the density penalty parameter, which is set to 3 in the present work.

In sum, the continuous design variables $\phi_1(\vec{x})$, and $\phi_2(\vec{x})$ in (2) determine the magnitude of PM remanence $\vec{B}_r(\vec{x})$, and the relative magnetic permeability $\mu_r(\vec{x})$ using the multi-material interpolation formulation in (7) and (8). The region where $\rho_1 = 1$ and $\rho_2 = 0$ represents a PM material, while the region where $\rho_1 = 1$ and $\rho_2 = 1$ represents a back-iron material. The region where $\rho_1 = 0$ represents an air material regardless of the value of ρ_2. In addition, the PM magnetization direction (i.e. direction of $\vec{B}_r(\vec{x})$) is determined by the orientation vector field $\vec{\vartheta}(\vec{x})$ in (6) that is controlled by design variables $\zeta(\vec{x})$, and $\eta(\vec{x})$.

B. PENALIZATION SCHEME FOR PM FRAGMENTATION

A PM design result with continuously varying magnetization direction may be difficult to manufacture. A manufacturability can be assured, with a slight performance sacrifices, through a combination of segmented PM blocks with uniform magnetizations. For the design of segmented PM blocks, various approaches [7]–[16] have been proposed. Among various techniques, the present work applies a penalization scheme using the approximated minimum distance in [11]. In this scheme, the magnitude of PM remanence $\bar{B}_r$ in (7) is penalized using the weighting field $w(\vec{x}) \in [0, 1]$:

$$\bar{B}_r\big(\vec{\vartheta}(\vec{x})\big) = B_{PM}\, w(\vec{x}), \tag{9}$$

where B_{PM} is the remanence value of PM material. In (9), the weighting field $w(\vec{x})$ is defined as

$$w(\vec{x}) = R\big(1 - s\, d_{min}(\vec{x})\big), \tag{10}$$

where, R is the ramp function that is defined as $R(\cdot) = \max(\cdot, 0)$, and a positive real number s in (10) is the orientation penalty parameter that controls a penalty strength. In (10), a minimum distance field d_{min} in (10) is defined as

$$d_{min}(\vec{x}) = \min(d_i(\vec{x})), \quad i = 1, 2, \ldots, n, \tag{11}$$

where $d_i(\vec{x})$ is defined as the distance between orientation vector field $\vec{\vartheta}(\vec{x})$ in (6) and n number of discrete target direction vector $\vec{v}_i = [v_i^x\ v_i^y]^{\mathrm{T}}$:

$$d_i(\vec{x}) = \|\vec{\vartheta}(\vec{x}) - \vec{v}_i\|, \quad i = 1, 2, \ldots, n. \tag{12}$$

To apply a gradient-based optimization algorithm, a minimum function in (11) is approximated using the p-norm:

$$d_{min}(\vec{x}) \approx \Big[\sum_{i=1}^{n}\Big(\frac{1}{d_i(\vec{x}) + \epsilon_0}\Big)^{P_{nm}}\Big]^{\frac{1}{P_{nm}}}, \quad i = 1, 2, \ldots, n, \tag{13}$$

where ϵ_0 is an infinitesimal number to avoid the singular point, and P_{nm} is a positive integer parameter.

The working principle of the penalization scheme by (9)-(13) is as follows. The PM remanence $\bar{B}_r$ in (9) is penalized at the location $\vec{x}$ where the orientation vector $\vec{\vartheta}(\vec{x})$ is far from any of the discrete target vector $\vec{v}_i$. On the other hand, no penalty is applied at the location $\vec{x}$ where the orientation vector $\vec{\vartheta}(\vec{x})$ is aligned with any of the discrete target vector $\vec{v}_i$. To avoid a penalization in PM strength, the orientation vector $\vec{\vartheta}$ moves into target discrete magnetization directions $\vec{v}_i$ during optimization iterations. Consequently, a PM design with continuously varying magnetization direction is altered into

a combination of PM blocks whose magnetization directions are aligned with discrete target directions $\vec{v}_i$.

In the penalization scheme in [11], the discrete target direction vector $\vec{v}_i$ is not fixed, but optimized together during a topology optimization procedure. Instead of directly using $\vec{v}_i$ as design variables, the vectors $\boldsymbol{\tau}_i = [\tau_i^x \ \tau_i^y]^{\mathrm{T}}$, $i = 1, 2, \ldots, n$ with bounds $\tau_i^x \in [-1, 1]$, $\tau_i^y \in [-1, 1]$ are utilized as additional design variables. The relation between $\vec{v}_i$ and $\boldsymbol{\tau}_i$ is given as

$$\vec{v}_i = \begin{bmatrix} v_i^x \\ v_i^y \end{bmatrix} = \frac{1}{\|\boldsymbol{\tau}_i\| + \epsilon_0} \begin{bmatrix} \tau_i^x \\ \tau_i^y \end{bmatrix}, \quad i = 1, 2, \ldots, n. \tag{14}$$

where ϵ_0 is an infinitesimal number to avoid the singular point, which is set to 10^{-6} in the present work. The direction vector $\vec{v}_i$ defined in (14) automatically satisfy the unity magnitude condition (i.e. $\|\vec{v}_i\| = \sqrt{(v_i^x)^2 + (v_i^y)^2} = 1$) without additional constraints. The unity magnitude condition is required for the orientation representation in a Cartesian coordinate system.

C. OPTIMIZATION STRATEGY

Segmented PM blocks together with back-iron structure are simultaneously designed by solving the optimization problem, which is formulated as

$$\begin{aligned} &\text{Find} && \vec{d}(\vec{x}), \text{and } \boldsymbol{\tau}_i && (15)\\ &\text{Maximize} && \Phi\big(\vec{A}(\vec{d}(\vec{x})), \vec{d}(\vec{x}), \boldsymbol{\tau}_i\big) && (16)\\ &\text{Subject to} && \vec{K}(\vec{d}(\vec{x}))\vec{A} = \mathbf{f}(\vec{d}(\vec{x}), \boldsymbol{\tau}_i) && (17)\\ & && V_{PM}\big(\vec{d}(\vec{x})\big) \le V_{PM}^* && (18)\\ & && V_{iron}\big(\vec{d}(\vec{x})\big) \le V_{iron}^*. && (19) \end{aligned}$$

As shown in (15), the design variables of the optimization problem includes not only the topology optimization vector field $\vec{d}(\vec{x})$ in (2), but also the vector variable for target magnetization directions of PM blocks $\boldsymbol{\tau}_i$ in (14). The objective functional, Φ, in (16), may be a function of the magnetic vector potential field, $\vec{A}(\vec{x})$, design variable vector field $\vec{d}(\vec{x})$, and discrete target direction vector $\boldsymbol{\tau}_i$. The first constraint in (17) is derived from the magnetostatic governing equation (1) by finite element formulation. In (17), $\vec{K}$ is the stiffness matrix, and $\vec{f}$ is the force vector. Additionally, the total volumes of the PM and back-iron materials, V_{PM}, and V_{iron} are restricted less than target volumes V_{PM}^* and V_{iron}^*, respectively. The total volumes are calculated as the integral of two material density fields $\rho_1(\vec{x})$ and $\rho_2(\vec{x})$ in (4) in a design domain Ω_D:

$$V_{PM}\big(\vec{d}(\vec{x})\big) = \int_{\Omega_D} \rho_1(\vec{x})\big(1 - \rho_2(\vec{x})\big)dV, \tag{20}$$

$$V_{iron}\big(\vec{d}(\vec{x})\big) = \int_{\Omega_D} \rho_1(\vec{x})\rho_2(\vec{x})dV. \tag{21}$$

The optimization problem (15)-(19) is solved using the Globally Convergent Method of Moving Asymptotes (GCMMA) [23], [24] implemented in MATLAB with COMSOL V5.5. In the GCMMA, the maximum number of inner iterations is set as 8. During the optimization iteration, a continuation scheme is applied for the bandwidth parameter h in (5) and orientation penalty parameter s in (10). The bandwidth parameter h starts with 1 and decreases by 0.04 for every 4 steps after the convergence criterion is satisfied. The convergence criterion is defined using two relative errors of objective functions (refer to [11]). As the parameter h decreases, the material density fields converged into black and white (i.e. zero-one) design. The orientation penalty parameter s starts with zero and increases by 0.04 for every 4 steps after the convergence criteria is satisfied. As the parameter s increases, continuous PM magnetization directions converge into the discrete target magnetization directions, which result in segmented PM array design. (refer to the continuous and discrete orientation design scheme in [25]). The optimization iteration stops when the bandwidth, h, decreases by less than 0.4.

D. POST-PROCESSING FOR NON-MAGNETIC FRAME STRUCTURE DESIGN

In the present work, a post-processing scheme is proposed for the design of a non-magnetic frame structure. As shown in Fig. 1, topology optimization result is composed of several PM and back-iron blocks. In order to tie PM and back-iron blocks tightly, a frame structure surrounding the blocks is designed through a post-processing scheme. In addition, the shape of PM and back-iron blocks are adjusted to fit a designed frame through the proposed scheme. The detailed formulations of a post-processing scheme is as follows.

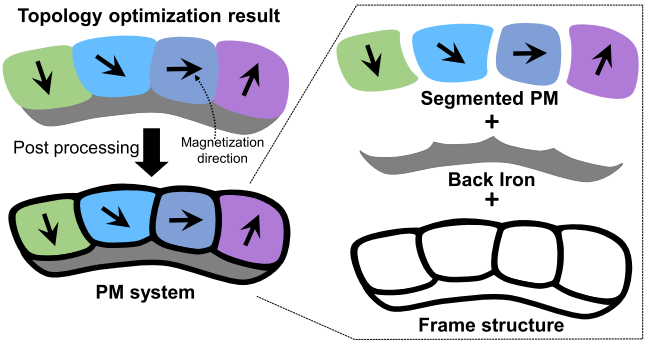

FIGURE 1. Post-processing for design of a magnetic system composed of segmented PM, back-iron, and fram structure.

In the proposed scheme, a frame structure is designed as a boundary of different PM and back-iron blocks. Here, the boundary is identified from smoothed density fields, which are obtained by applying a Helmholtz filtering [20], [21] to density fields that representing PM and back-iron blocks. In order to define the density field for each segmented PM block, angles located in the middle of optimized discrete magnetization directions $\vec{v}_i$ are first computed as shown in Fig. 2. From the arctangent function of the optimized target directions $\vec{v}_i$, the angles are computed and sorted in ascending order, which results in $\theta_i \in [-\pi, \pi]$, $i = 1, 2, \ldots, n$. Here n is the total number of discrete target magnetization directions. Next, The intermediate angles between θ_i are computed and sorted in ascending order, which

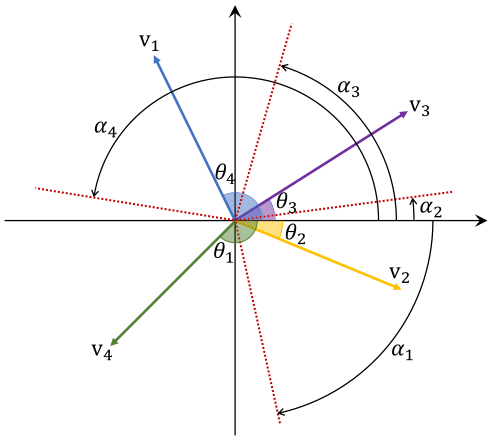

FIGURE 2. Intermediate angles α_i between optimized magnetization directions $\vec{v}_i$, which are prepared to define density fields ρ_i^{PM} representing segmented PM blocks.

gives $\alpha_i \in [-\pi, \pi]$, $i = 1, 2, \ldots, n$, as shown in Fig. 2. From the angles α_i, the density $\rho_i^{PM}(\vec{x})$ for segmented PM blocks are defined as

$$\rho_i^{PM}(\vec{x}) = \begin{cases} \left[H\left(\arctan(\frac{\vartheta_y}{\vartheta_x}) - \alpha_i\right) H\left(\alpha_{i+1} - \arctan(\frac{\vartheta_y}{\vartheta_x})\right)\right]\rho_1(1-\rho_2) \\ \text{for } i = 1, 2, \ldots, n-1 \\ \left[H\left(\arctan(\frac{\vartheta_y}{\vartheta_x}) - \alpha_i\right) + H\left(\alpha_1 - \arctan(\frac{\vartheta_y}{\vartheta_x})\right)\right]\rho_1(1-\rho_2) \\ \text{for } i = n \end{cases} \tag{22}$$

where H is the Heaviside step function, ϑ_x and ϑ_y are the component of the orientation vector field $\boldsymbol{\vartheta}(\vec{x})$ in (6), ρ_1 and ρ_2 is material density fields in (4). In addition, the density field ρ^{iron} representing back-iron blocks are defined as

$$\rho^{iron}(\vec{x}) = \rho_1 \rho_2 \tag{23}$$

Next, the smoothed density fields $\tilde{\rho}_i^{PM}(\vec{x})$ and $\tilde{\rho}^{iron}(\vec{x})$ are obtained from a Helmholtz filtering:

$$-R_{PM}^2 \begin{bmatrix} \nabla^2\tilde{\rho}_1^{PM}(\vec{x}) \\ \nabla^2\tilde{\rho}_2^{PM}(\vec{x}) \\ \vdots \\ \nabla^2\tilde{\rho}^{iron}(\vec{x}) \end{bmatrix} + \begin{bmatrix} \tilde{\rho}_1^{PM}(\vec{x}) \\ \tilde{\rho}_2^{PM}(\vec{x}) \\ \vdots \\ \tilde{\rho}^{iron}(\vec{x}) \end{bmatrix} = \begin{bmatrix} \rho_1^{PM}(\vec{x}) \\ \rho_2^{PM}(\vec{x}) \\ \vdots \\ \rho^{iron}(\vec{x}) \end{bmatrix}, \tag{24}$$

where R_{PM} is a filter radius. From the smoothed density fields $\tilde{\rho}_i^{PM}(\vec{x})$ and $\tilde{\rho}^{iron}(\vec{x})$, a density field that representing frame structure, $\hat{\tilde{\rho}}^{frame}(\vec{x})$ is defined as

$$\hat{\tilde{\rho}}^{frame}(\vec{x}) = \sum_{i=1}^{n}\left[H(\tilde{\rho}_i^{PM} - 0.3)H(0.7 - \tilde{\rho}_i^{PM})\right] + H(\tilde{\rho}_i^{iron} - 0.3)H(0.7 - \tilde{\rho}_i^{iron}). \tag{25}$$

In addition, density fields for PM and back-iron blocks that are adjusted to fit into a frame structure, $\hat{\tilde{\rho}}_i^{PM}(\vec{x})$, $i = 1, 2, \ldots, n$, and $\hat{\tilde{\rho}}^{iron}(\vec{x})$ are defined as

$$\hat{\tilde{\rho}}_i^{PM}(\vec{x}) = H(\tilde{\rho}_i^{PM} - 0.7), \tag{26}$$

$$\hat{\tilde{\rho}}^{iron}(\vec{x}) = H(\tilde{\rho}^{iron} - 0.7). \tag{27}$$

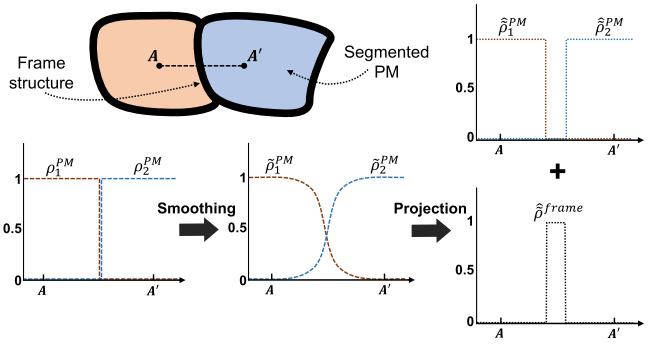

FIGURE 3. Smoothing and projection procedures for density fields $\hat{\tilde{\rho}}^{frame}(\vec{x})$, and $\hat{\tilde{\rho}}_i^{PM}(\vec{x})$ that representing frame structure and adjusted PM blocks, respectively.

Fig. 3 exhibits the density fields along the line AA' in the example result. In the figure, ρ_1^{PM} and ρ_2^{PM} represents segmented PM blocks with different magnetization directions. From their smoothed variables $\tilde{\rho}_1^{PM}$ and $\tilde{\rho}_2^{PM}$, the density field for a frame structure $\hat{\tilde{\rho}}^{frame}$ are acquired together with adjusted PM blocks $\hat{\tilde{\rho}}_1^{PM}$, and $\hat{\tilde{\rho}}_2^{PM}$. The final designs of a frame, PM and iron structures are extracted as the region where $\hat{\tilde{\rho}}^{frame}(\vec{x})$, $\hat{\tilde{\rho}}_i^{PM}(\vec{x})$ and $\hat{\tilde{\rho}}^{iron}(\vec{x})$ are one, respectively.

III. FABRICATION OF DESIGN RESULT

Through multi-material topology optimization explained in Section II, density fields representing segmented PM blocks, back-iron, and frame structures are obtained as the final result. From the obtained density fields, CAD models are prepared for the fabrication of each component. Taking manufacturing costs and material characteristics into consideration, each component is fabricated using conventional or additive manufacturing techniques.

Segmented PM blocks are made of Barium ferrite (MPB380). Ferrite materials have high hardness, but easy to brittle. Common methods of manufacturing ferrite magnets include injection molding, diamond blade cutting, water-jet cutting. In injection molding, a part is produced by injecting molten material into a mold prepared in a desired shape. Although it has the advantage of being able to mass-produce parts with complex shapes, it is expensive and time-consuming for preparing a mold structure. Diamond blade cutting has limitations in processing complex shapes designed by topology optimization. Water-jet cutting can process complex shapes of various materials, and it does not require additional efforts like mold structure preparation. Thus, water-jet cutting is utilized for segmented PM fabrication in the present work. The water-jet equipment model used for PM fabrication is TOPS SJA-2040 with cutting area

4,000 mm × 2,000 mm × 200 mm and machine accuracy ±0.03 mm.

Back-iron structures designed from topology optimization is made of low-carbon steel (JIS G3101). Low carbon steel has good workability in manufacturing, and thus it can be processed by various conventional manufacturing methods such as milling machining, laser/plasma cutting, and electrical discharge machining (EDM). In the present work, a wire electrical discharge machining (wire EDM) is applied for the fabrication of back-iron structure. A wire EDM enables high-precision processing of high electric-conductivity materials (i.e. metals) regardless of its mechanical characteristics. It has the advantages of easy processing of complex shapes and less thermal surface deterioration. In the present work, back-iron structures are fabricated using a wire EDM machine (Model: Seibu M750) with working area $750mm \times 500mm \times 310mm$ and machine accuracy $\pm 0.001mm$.

A frame structure is intended to bind segmented PM and back-iron blocks, and thus it is made of non-magnetic material. In the present work, additive manufacturing is used for the fabrication of frame structures considering manufacturing convenience. Specifically, additive manufacturing is performed using a multi-jet printing machine (model: 3D Systems Projet 3510 SD) with a resolution of 0.025-0.05 mm per 25.4 mm. As a printing material, ultraviolet curing plastic (Visijet M3 Crystal) is utilized in the present work.

IV. DESIGN AND FABRICATION EXAMPLES

This section provides two design and fabrication examples of magnetic system. The first example aims to design a magnetic system for maximizing the magnetic field inside a rectangular cavity. In the second example, a magnetic system is designed for maximizing the magnetic force generated with a C-core electromagnet.

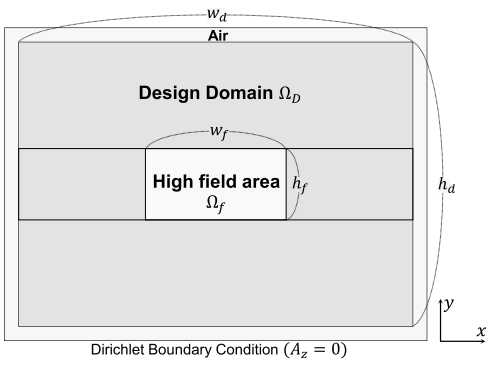

FIGURE 4. Example 1 – Design domain Ω_D, and high field area Ω_f with boundary condition.

A. MAGNETIC SYSTEM WITH RECTANGULAR CAVITY

Fig. 4 shows the design domain Ω_D, high field area Ω_f with boundary conditions of the first design example. The design domain width w_d, and height h_d are set to 210 mm, and 150 mm, respectively. The high field area width w_f and height h_f are set to 75 mm, and 37.5 mm, respectively. The representative element size is set to 1.5 mm. The filter radii R_ϕ in (3) and R_{PM} in (24) are set to the same value as the representative element size (i.e. 1.5 mm). The remanence value of PM material B_{PM} in (9) is set to 1.2 T in this example. The initial values of design variable vector fields $\vec{d}(\vec{x}) = [\phi_1\ \phi_2\ \zeta\ \eta]^{\mathrm{T}}$ in (15) are set to $[0\ 0\ -0.9\ -1]^{\mathrm{T}}$, respectively. The objective function Φ in (16) is set as an averaged y-directional magnetic flux density B_y in the high field area Ω_f:

$$\Phi = \frac{1}{V_f}\int_{\Omega_f} B_y dV, \tag{28}$$

where V_f is the volume of the high field area. The target volumes V^*_{PM} (18) and V^*_{iron} in (19) are set to 0.25 and 0.1, respectively. The total number of discrete target magnetization directions, n, is set as four in this example, and the initial directions of $\boldsymbol{\tau}_i$ in (15) is set as evenly distributed vectors.

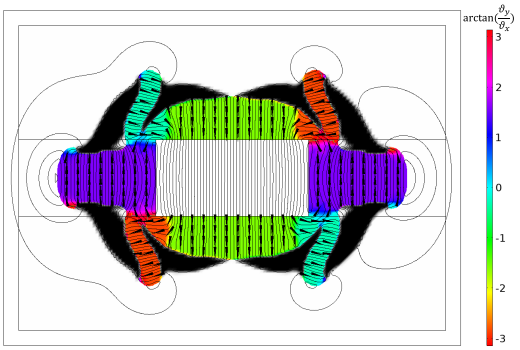

FIGURE 5. Example 1 – Segmented PMs and back-iron structure designed for maximizing y-directional magnetic field inside a rectangular cavity.

Fig. 5 presents a magnetic system design result obtained by multi-material topology optimization. In Fig. 5, black color represents the back-iron material, and the colored region represents the PM material. The color of the PM region indicates the magnetization directions that is calculated as the arctangent function of ϑ_y and ϑ_x in (6). The black-colored arrows in the PM regions shows the direction of the magnetization direction. The contour lines represent the equipotential lines showing the direction and magnitude of the magnetic flux density. From the equipotential lines, it is confirmed that designed segmented PM and back-iron blocks successfully maximize the averaged y-directional magnetic flux density B_y in the high field area Ω_f. The objective function (i.e averaged B_y in the high field area Ω_f) of the design result in Fig. 5 is calculated as 0.7516 T.

For fabrication, the design result in Fig. 5 is post-processed by the scheme explained in Section II-D. Fig. 6(a) shows the post-processed design result. In Fig. 6(a), the black-colored thin structure represents the frame structure extracted by the density field $\hat{\tilde{\rho}}^{frame}(\vec{x})$ in (25). In addition, the colored region represents adjusted PM blocks extracted by the field $\hat{\tilde{\rho}}^{PM}_i(\vec{x})$ in (26), and the gray region represents adjusted

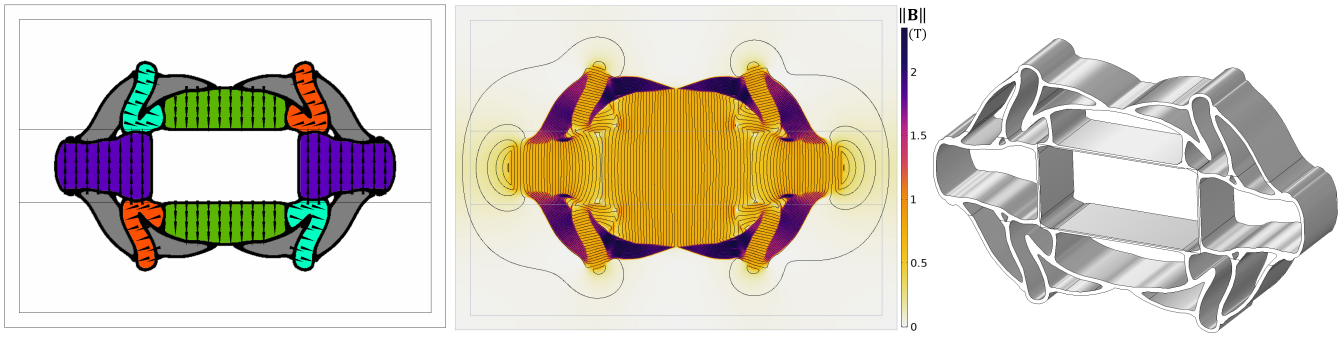

FIGURE 6. Example 1 – (a) Post-processed final design result, (b) Distribution plot of magnetic flux density magnitude $\|\vec{B}\|$ with equipotential lines, (c) CAD model of a frame structure that is extracted from the density field $\hat{\tilde{\rho}}^{frame}(\vec{x})$ in (25).

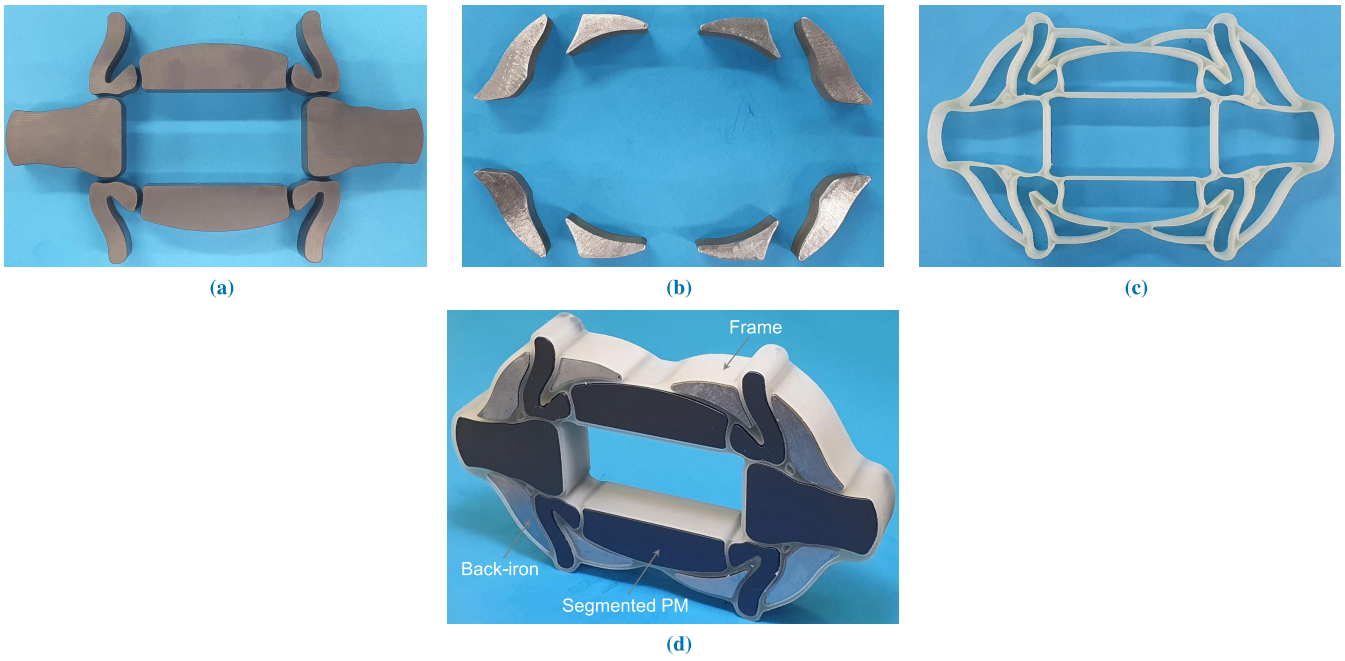

FIGURE 7. Example 1 – Fabrication results: (a) Segmented PM blocks, (b) Back-iron structure, (c) Frame structure, and (d) Assembled magnetic system.

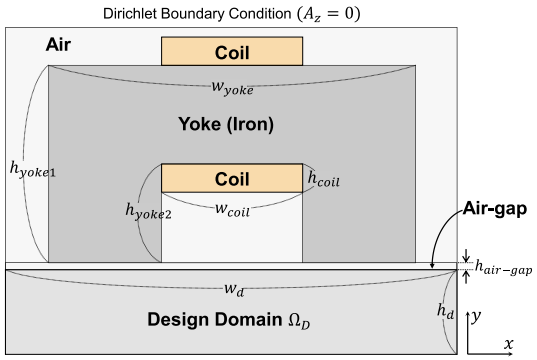

FIGURE 8. Example 2 – Design domain Ω_D with boundary condition.

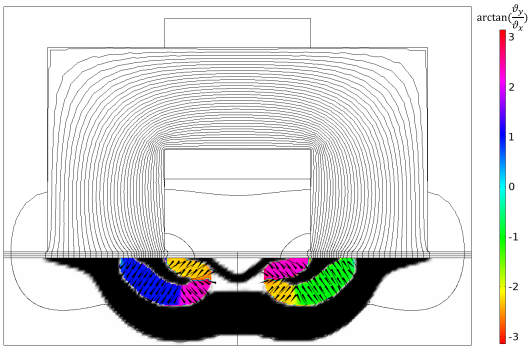

FIGURE 9. Example 2 – Segmented PMs and back-iron structure designed for maximizing y-directional magnetic force.

back-iron structure by the density field $\hat{\tilde{\rho}}^{iron}(\vec{x})$ in (27). The black-colored arrow represents the optimized four magnetization directions $\vec{v}_i$ in (14). As shown in Fig. 6(a), the proposed post-processing scheme successfully modifies topology optimization result into a magnetic system composed of a non-magnetic frame structure, segmented PMs,

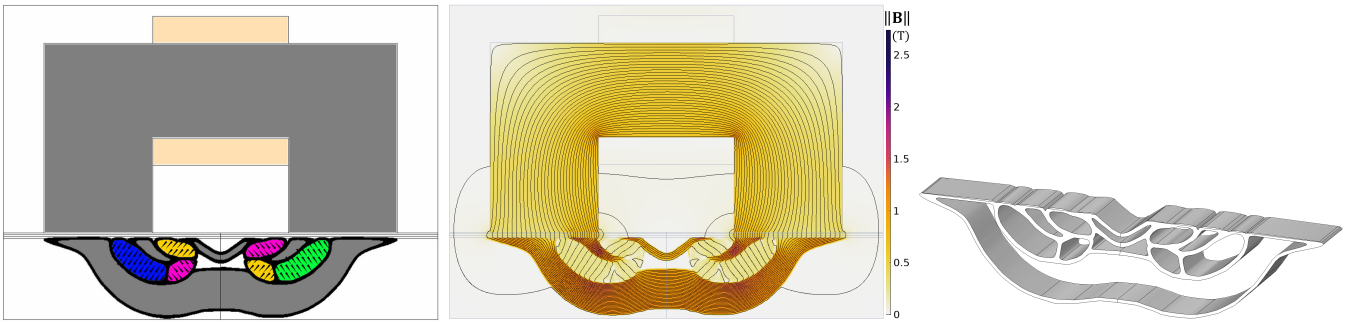

FIGURE 10. Example 2 – (a) Post-processed design result, (b) Distribution plot of magnetic flux density magnitude $\|\vec{B}\|$ with equipotential lines, (c) CAD model of a frame structure that is extracted from the density field $\hat{\tilde{\rho}}^{frame}(\vec{x})$ in (25).

and back-iron structure. Fig. 6(b) shows the distribution of the magnetic flux density magnitude $\|\vec{B}\|$, which is obtained by the re-analysis of the post-processed design result. After the re-analysis, the averaged y-directional magnetic flux density B_y in the high field area Ω_f is calculated as 0.6920 T, which is 7.93% lower than the original value (i.e. 0.7516 T) of the design result before the post-processing. The decrease in the averaged B_y might because PM and iron materials at interfaces are changed into non-magnetic frame structure in the post-processing procedure. The post-processed final design result is converted into CAD models for fabrication. Fig. 6(c) shows the CAD model of a frame structure, which is extruded with 0.03m thickness from the final design result.

Three components of the design result (i.e. segmented PMs, back-iron, and frame-structure) are processed using the manufacturing techniques described in Section III. Figs. 7(a)-(c) show the fabrication results of PMs, back-iron, and frame-structure, respectively. Each component is processed as desired. Fig. 7(d) shows the final fabrication result that is obtained by assembling the three components. Through comparing the design result in Fig. 6(a) and the fabrication result in Fig. 7(d), it is confirmed that a magnetic system designed using topology optimization can be manufactured.

B. MAGNETIC SYSTEM FOR MAGNETIC FORCE MAXIMIZATION

Fig. 4 shows the design domain Ω_D with boundary conditions of the second design example. In the second example, a C-core electromagnet consisting of yoke and coils is located above the design domain Ω_D. The design domain width w_d, and height h_d are set to 240 mm, and 45 mm, respectively. The dimensions for the yoke and coil parts, w_{yoke}, h_{yoke1}, h_{yoke2}, w_{coil}, and h_{coil} are set to 195 mm, 105mm, 52.5 mm, 75 mm, 15mm, respectively. The air-gap length $h_{air-gap}$ is set to 3.5 mm. The representative element size is set to 1.5 mm. The filter radii R_ϕ in (3) and R_{PM} in (24) are set to the same value as the representative element size (i.e. 1.5 mm). The remanence value of PM material B_{PM} in (9) is set to 0.4 T in this example. In the coil regions, the external current is set to 40 A with 30 number of coil turns. The initial values of design variable vector fields $\vec{d}(\vec{x}) = [\phi_1\ \phi_2\ \zeta\ \eta]^{\mathrm{T}}$ in (15) are set to $[0\,0\,-0.6\,-0.8]^{\mathrm{T}}$, respectively. The objective function Φ in (16) is set as y-directional magnetic force F_y acting on the design domain, which is calculated by the Maxwell stress tensor formulation:

$$\Phi = F_y = \oint \frac{1}{2\mu_0}(B_y^2 - B_x^2)\, dl, \tag{29}$$

where μ_0 is the air permeability, B_y and B_x are y and x components of the magnetic flux density. In (29), the line integral is performed along a closed line surrounding the design domain. The target volumes V_{PM}^* (18) and V_{iron}^* in (19) are set to 0.35 and 0.15, respectively. The total number of discrete target magnetization directions, n, is set as four in this example, and the initial directions of $\boldsymbol{\tau}_i$ in (15) is set as evenly distributed vectors.

A magnetic system designed for the magnetic force maximization is shown in Fig. 9. As with the previous design result, black and colored regions in Fig. 9 represent the back-iron and PM material, respectively. The color of the PM region, together with the black-colored arrow indicate the magnetization directions. In the design result of Fig. 9, the objective function (i.e y-directional magnetic force F_y) is calculated as 153.29 N. A strong magnetic force is generated by the combination of a C-core electromagnet and optimized back-iron and PM blocks.

A post-processed design result is shown in Fig. 10(a). As with the previous post-processed design result, the black-colored thin structure in Fig. 10(a) represents the frame structure, and colored region presents adjusted PM blocks. In addition, the gray region in the design domain represents adjusted back-iron block. Fig. 10(a) confirms that manufacturable design result can be obtained by the proposed post-processing scheme. Fig. 10(b) presents the distribution of the magnetic flux density magnitude $\|\vec{B}\|$, which is obtained by the re-analysis of the post-processed design result. From the re-analysis, the y-directional magnetic force F_y is calculated as 130.16 N, which is 15.1% lower than the original value (i.e. 153.29 N) of the design result before the post-processing. The reason for the considerable reduction of the magnetic

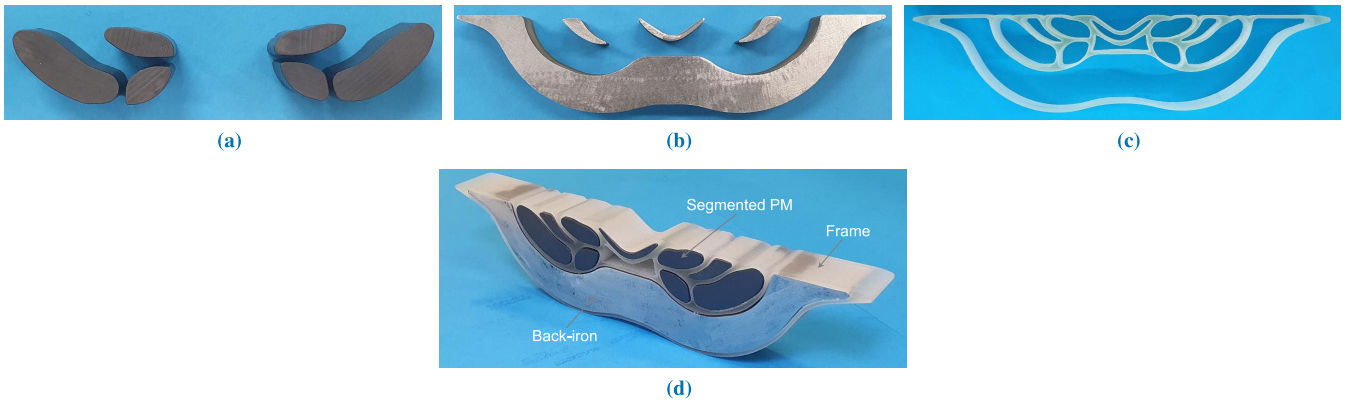

FIGURE 11. Example 2 – Fabrication results: (a) Segmented PM blocks, (b) Back-iron structure, (c) Frame structure, and (d) Assembled magnetic system.

force might be due to design changes near the air-gap that is sensitive region to the magnetic force. At the expense of magnetic force, a manufacturable magnetic system is successfully designed through a post-process procedure. The post-processed final design result is converted into CAD models for fabrication. Fig. 10(c) shows the CAD model of a frame structure, which is extruded with 0.03m thickness from the final design result.

Three components of the design result (i.e. segmented PMs, back-iron, and frame-structure) are processed using the manufacturing techniques described in Section III. Figs. 11(a)-(c) show the fabrication results of PMs, back-iron, and frame-structure, respectively. Each component is processed as desired. Fig. 11(d) shows the final fabrication result that is obtained by assembling the three components. Through comparing the design result in Fig. 10(a) and the fabrication result in Fig. 11(d), it is confirmed that a magnetic system designed using topology optimization can be manufactured.

V. CONCLUSION

This paper aims to present the design and fabrication of a magnetic system consisting of segmented PM blocks, back-iron and frame structures. A design approach based on multi-material topology optimization is proposed, and design results are fabricated using conventional and additive manufacturing techniques. Via two examples, the effectiveness of the proposed design and fabrication schemes was successfully validated. The first example aims to maximize the magnetic field inside a rectangular cavity, and the second example aims to maximize the magnetic force generated with C-core electromagnet. In both examples, segmented PMs, and back iron were successfully designed using a three-field density approach with an orientation penalization scheme. Subsequently, non-magnetic frame structures with adjusted PMs and back-irons (i.e. final design results) were obtained using a post-processing scheme based on the smoothed density fields. The re-analysis of final design results shows that performance deterioration due to design change for frame structure is acceptable. The final design results were converted into CAD format file, and fabricated using conventional and additive manufacturing techniques. Segmented PMs were made of Barium ferrite, and fabricated using a water-jet machining. Back irons were made of low-carbon steel, and fabricated using a wire EDMs. Frame structures were fabricated by additive manufacturing using a multi-jet printing machine with ultraviolet curing plastic material. The present work is limited in that the experimental validation is not carried out. Thus, future work will focus on the experimental studies, along with strategies for PM magnetization. In addition, the proposed design and fabrication schemes will be extended to electric machine application as future work.

REFERENCES

[1] M. P. Bendsøe and N. Kikuchi, "Generating optimal topologies in structural design using a homogenization method," *Comput. Methods Appl. Mech. Eng.*, vol. 71, no. 2, pp. 197–224, Nov. 1988.
[2] E. M. Dede, J. Lee, and T. Nomura, *Multiphysics Simulation: Electromechanical System Applications and Optimization*. London, U.K.: Springer, 2016.
[3] X. Duan, Y. Dang, and J. Lu, "A variational level set method for topology optimization problems in Navier-Stokes flow," *IEEE Access*, vol. 8, pp. 48697–48706, 2020.
[4] Q. Yuan, S. Qu, H. Ma, S. Sui, Y. Shen, J. Wang, M. Feng, H. Chen, Y. Jin, and X. Wang, "A broadband wide-angle synthetical absorber designed by topology optimization of resistance surface and metal wires," *IEEE Access*, vol. 7, pp. 142675–142681, 2019.
[5] S.-H. Zhu, X.-S. Yang, J. Wang, N.-S. Nie, and B.-Z. Wang, "Mutual coupling reduction of ±45° dual-polarized closely spaced MIMO antenna by topology optimization," *IEEE Access*, vol. 8, pp. 29089–29098, 2020.
[6] J.-S. Choi and J. Yoo, "Design of a Halbach magnet array based on optimization techniques," *IEEE Trans. Magn.*, vol. 44, no. 10, pp. 2361–2366, Oct. 2008.
[7] J. S. Choi and J. Yoo, "Optimal design method for magnetization directions of a permanent magnet array," *J. Magn. Magn. Mater.*, vol. 322, no. 15, pp. 2145–2151, Aug. 2010.
[8] J. Lee, T. Nomura, and E. M. Dede, "Topology optimization of Halbach magnet arrays using isoparametric projection," *J. Magn. Magn. Mater.*, vol. 432, pp. 140–153, Jun. 2017.
[9] R. Teyber, P. V. Trevizoli, T. V. Christiaanse, P. Govindappa, and A. Rowe, "Topology optimization of reduced rare-Earth permanent magnet arrays with finite coercivity," *J. Appl. Phys.*, vol. 123, no. 19, May 2018, Art. no. 193903.
[10] A. R. Insinga, A. Smith, C. R. H. Bahl, K. K. Nielsen, and R. Bjørk, "Optimal segmentation of three-dimensional permanent-magnet assemblies," *Phys. Rev. A, Gen. Phys. Appl.*, vol. 12, no. 6, Dec. 2019, Art. no. 064034.
[11] J. Lee, J. Lee, T. Jung, and J. Yoo, "Topology optimization for three-dimensional design of segmented permanent magnet arrays," *Struct. Multidisciplinary Optim.*, vol. 62, no. 6, pp. 3089–3104, Dec. 2020.

[12] R. Bjørk, C. R. H. Bahl, and A. R. Insinga, "Topology optimized permanent magnet systems," *J. Magn. Magn. Mater.*, vol. 437, pp. 78–85, Sep. 2017.
[13] R. Teyber, P. V. Trevizoli, T. V. Christiaanse, P. Govindappa, I. Niknia, and A. Rowe, "Permanent magnet design for magnetic heat pumps using total cost minimization," *J. Magn. Magn. Mater.*, vol. 442, pp. 87–96, Nov. 2017.
[14] R. Bjørk and A. R. Insinga, "A topology optimized switchable permanent magnet system," *J. Magn. Magn. Mater.*, vol. 465, pp. 106–113, Nov. 2018.
[15] J. Lee, M. Yoon, T. Nomura, and E. M. Dede, "Topology optimization for design of segmented permanent magnet arrays with ferromagnetic materials," *J. Magn. Magn. Mater.*, vol. 449, pp. 571–581, Mar. 2018.
[16] J. Lee, S.-W. Lee, K. Kim, and J. Lee, "Multi-material topology optimization of magnetic actuator with segmented permanent magnets," *IEEE Trans. Magn.*, vol. 54, no. 7, Jul. 2018, Art. no. 8202706.
[17] C. Huber, C. Abert, F. Bruckner, C. Pfaff, J. Kriwet, M. Groenefeld, I. Teliban, C. Vogler, and D. Suess, "Topology optimized and 3D printed polymer-bonded permanent magnets for a predefined external field," *J. Appl. Phys.*, vol. 122, no. 5, Aug. 2017, Art. no. 053904.
[18] C. Huber, M. Goertler, C. Abert, F. Bruckner, M. Groenefeld, I. Teliban, and D. Suess, "Additive manufactured and topology optimized passive shimming elements for permanent magnetic systems," *Sci. Rep.*, vol. 8, no. 1, p. 14651, Dec. 2018.
[19] R. Wrobel and B. Mecrow, "A comprehensive review of additive manufacturing in construction of electrical machines," *IEEE Trans. Energy Convers.*, vol. 35, no. 2, pp. 1054–1064, Jun. 2020.
[20] A. Kawamoto, T. Matsumori, S. Yamasaki, T. Nomura, T. Kondoh, and S. Nishiwaki, "Heaviside projection based topology optimization by a PDE-filtered scalar function," *Struct. Multidisciplinary Optim.*, vol. 44, no. 1, pp. 19–24, Jul. 2011.
[21] B. S. Lazarov and O. Sigmund, "Filters in topology optimization based on Helmholtz-type differential equations," *Int. J. Numer. Methods. Eng.*, vol. 86, no. 6, pp. 765–781, 2011.
[22] J. R. Brauer, "Simple equations for the magnetization and reluctivity curves of steel," *IEEE Trans. Magn.*, vol. 11, no. 1, p. 81, Jan. 1975.
[23] K. Svanberg, "The method of moving asymptotes—A new method for structural optimization," *Int. J. Numer. Methods Eng.*, vol. 24, no. 2, pp. 359–373, 1987.
[24] K. Svanberg, "A class of globally convergent optimization methods based on conservative convex separable approximations," *SIAM J. Optim.*, vol. 12, no. 2, pp. 555–573, Jan. 2002.
[25] J. Lee, D. Kim, T. Nomura, E. M. Dede, and J. Yoo, "Topology optimization for continuous and discrete orientation design of functionally graded fiber-reinforced composite structures," *Compos. Struct.*, vol. 201, pp. 217–233, Oct. 2018.

TAEHOON JUNG received the B.S. degree in mechanical design engineering from Jeonbuk National University, South Korea, in 2016, and the M.S. degree in mechanical engineering from the Gwangju Institute of Science and Technology (GIST), South Korea, in 2018, where he is currently pursuing the Ph.D. degree in mechanical engineering. His current research interest includes the design and manufacturing of electric machines.

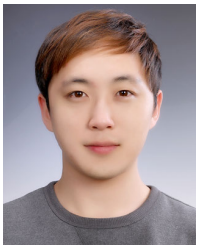

JAEJOON LEE received the B.S. and M.S. degrees in mechanical engineering from Korea Aerospace University, South Korea, in 2016 and 2018, respectively. He is currently pursuing the Ph.D. degree in mechanical engineering from the Gwangju Institute of Science and Technology (GIST), South Korea. His current research interests include the development of numerical analysis and design optimization methods for the vibration reduction of electric motors.

JAEWOOK LEE received the B.S. degree in naval architecture and ocean engineering from Seoul National University, South Korea, in 2004, and the M.S. and Ph.D. degrees in mechanical engineering from the University of Michigan, Ann Arbor, MI, USA, in 2006 and 2010, respectively.

He was a Research Engineer with the Toyota Research Institute of North America, Ann Arbor. He is currently an Associate Professor with the School of Mechanical Engineering, Gwangju Institute of Science and Technology (GIST). His expertise covers multiphysics simulation and structural design optimization of electromechanical devices. His current research interest includes the development of numerical design optimization schemes for electric motor application.